# Directional shock diode behavior through the interaction of geometric voids in engineered polymer assemblies

Cite as: J. Appl. Phys. 128, 245903 (2020); https://doi.org/10.1063/5.0029835 Submitted: 17 September 2020 . Accepted: 13 November 2020 . Published Online: 30 December 2020

D Brittany A. Branch, Geoff Frank, Andrew Abbott, David Lacina, Dana M. Dattelbaum, Christopher Neel, and Jonathan Spowart







# ARTICLES YOU MAY BE INTERESTED IN

Shock compression of diamonds in silicon carbide matrix up to 110 GPa
Journal of Applied Physics 128, 245901 (2020); https://doi.org/10.1063/5.0033747

Boris computational spintronics—High performance multi-mesh magnetic and spin transport modeling software

Journal of Applied Physics 128, 243902 (2020); https://doi.org/10.1063/5.0024382

High permeability and low loss flaky carbonyl iron soft magnetic composite for 5G applications

Journal of Applied Physics 128, 244905 (2020); https://doi.org/10.1063/5.0033692





# Directional shock diode behavior through the interaction of geometric voids in engineered polymer assemblies

Cite as: J. Appl. Phys. **128**, 245903 (2020); doi: 10.1063/5.0029835 Submitted: 17 September 2020 · Accepted: 13 November 2020 · Published Online: 30 December 2020







Brittany A. Branch,<sup>1,a)</sup> © Geoff Frank,<sup>2,3</sup> Andrew Abbott,<sup>3,4</sup> © David Lacina,<sup>5</sup> Dana M. Dattelbaum,<sup>6</sup> © Christopher Neel,<sup>7</sup> and Jonathan Spowart<sup>3</sup>

## **AFFILIATIONS**

- <sup>1</sup>Sandia National Laboratories, Albuquerque, New Mexico 87123, USA
- <sup>2</sup>Applied Mechanics Division, University of Dayton Research Institute, Dayton, Ohio 45469, USA
- <sup>3</sup>Air Force Research Laboratory, Wright-Patterson Air Force Base, Ohio 45433, USA
- Structural Material Division, University of Dayton Research Institute, Dayton, Ohio 45469, USA
- <sup>5</sup>University of Dayton Research Insitute, Eglin Air Force Base, Florida 32542, USA
- <sup>6</sup>Los Alamos National Laboratory, Los Alamos, New Mexico 87545, USA
- <sup>7</sup>Air Force Research Laboratory, Munitions Directorate, AFRL RWMWS, Eglin Air Force Base, Florida 32542, USA

# **ABSTRACT**

With the advent of additive manufacturing (AM) techniques, a new class of shockwave mitigation and structural supports has been realized through the hierarchical assembly of polymer materials. To date, there have been a limited number of studies investigating the role of structure on shockwave localization and whether AM offers a means to tailor shockwave behavior. Of particular interest is whether the mesoscopic structure can be tailored to achieve shockwave properties in one direction of impact vs the other. Here, we illustrate directional response in engineered polymer foams. *In situ* time-resolved x-ray phase contrast imaging at the Advanced Photon Source was used to characterize these diode-like structures. This work offers a breakthrough in materials technology for the development of protective structures that require augmentation of shock in one direction while diminishing transmission in the opposite direction.

https://doi.org/10.1063/5.0029835

# INTRODUCTION

Polymer foams have been used as structural components for vibration damping and as shockwave mitigation barriers in a large number of industries, including automotive, aerospace, electronics, and defense, due to their lightweight nature and superior mechanical and insulating properties. Typically, in stochastic foams, the mechanical behavior observed in foams is a result of the non-uniform structure that consists of material and voids having a broad distribution in size, shape, thickness, connectedness, and topology. In some cases, tunability of properties can be achieved by varying the foam's overall porosity or relative density through the synthesis, but there are limited means of tailoring material response or behavior.

Unlike traditional foaming techniques, additive manufacturing (AM) provides a means to introduce microstructural control of topology to achieve material functionality that can be tailored toward an application. There are numerous examples of AM enabling materials development with unique conductive, acoustic, he thermal, and even multi-functional characteristics in polymer-based materials. Specifically, AM polymer materials with enhanced mechanical properties that affect deformation behavior relevant to structural components such as ductility, strength, or fracture toughness have been numerously reported. Le, 15, 16 More recently, the dynamic response of this class of materials under shockwave compression has been demonstrated. These effects include but are not limited to elastic deformation in AM lattices, 17

a)Author to whom correspondence should be addressed: babranc@sandia.gov

shockwave dynamics in periodic structures produced by AM and how they differ from stochastic polymer foams of similar density, <sup>18</sup> the shockwave modulation and graded shockwave dynamics in polymer architectures through the integration of intricate hierarchical microstructure, <sup>19</sup> the effect of pore geometry on the propagation of compression waves through polymer specimens with engineered porosity, <sup>20</sup> and more recently, the dissipative phenomena resulting from release wave interactions observed in shocked fractal polymers. <sup>21</sup> These high strain rate studies illustrate the revolutionary advances that AM offers in designing and realizing structural foams with unique elastic and plastic compressive responses as well as tailored localization phenomena resulting from internal structure.

Here, we use in situ, time-resolved x-ray phase contrast imaging (PCI) at the Advanced Photon Source<sup>22,23</sup> to demonstrate directional "shock diode" behavior in additively manufactured polymer foams. This work provides the basic testing and design of simple AM structures that demonstrate directional shockwave transmission behavior toward the development of a "shock diode." A "shock diode" concept could be envisioned in which the requirements of the diode would be one that shock transmission is largely dissipated or propagated depending on the direction of the shock input. This is analogous to an electrical diode where electrical transmission depends on the directional flow of current. Here, we report engineered structures that have different shockwave dynamics and localization phenomena as a result of the orientation of the AM structures relative to shock input. Although similar behavior could be achieved with graded density materials, <sup>24,25</sup> the directional behavior observed in the structures described here results from an initially planar shockwave interacting with discreet geometric voids engineered into a polymer assembly using AM, and subsequent void collapse results in a heterogeneous wave front that depends on the direction of impact. The unique capability utilizing x-ray phase contrast imaging coupled to dynamic events enable the real-time study of this interaction and the resulting shockwave propagation. We compare the experimentally measured shock behavior of the shock diode geometries to finite element analysis (FEA) performed using Abaqus.<sup>26</sup> Additionally, we report the principal Hugoniot for the PR48 photopolymer used with the Autodesk, Inc. Ember printer.<sup>27</sup> Future work developing a more rigorous "shock diode" concept will define an objective function that can be correlated to augment the

shock transmission in one direction while diminishing it in the other through geometric features or composite materials design.

#### **METHODS**

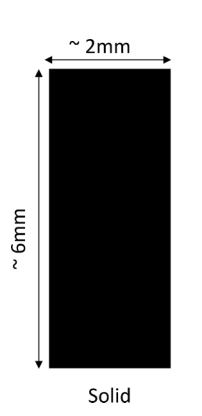
# Specimen fabrication

Specimens were fabricated by digital light projection (DLP) printing on an Ember printer (Autodesk, Inc.) using clear acrylic photopolymer resin PR48 (Colorado Photopolymer Solutions). An internal segmented mirror in the printer reflects a 405 nm ultraviolet light into the resin tray through a polydimethylsiloxane (PDMS) window partially curing one full layer. Mirror segments represent pixels and rotate independently in a binary fashion to project an image in each layer into the resin tray. The in-plane resolution is  $50\,\mu\mathrm{m}$  and the through-thickness resolution, termed layer height, was set to  $25\,\mu\mathrm{m}$ .

Three types of prismatic specimens were printed: solid bulk material printed to full density, a wedge geometry with sawtooth features, and a slot geometry with three distinct slit sizes arranged in increasing size across the part. All specimens were printed with target dimensions of 6 mm in length and width and 2 mm thick. All specimens were oriented such that the  $6\times 2$  mm face featuring the geometry of interest was in the XY plane. The first four layers were printed with an exposure time of 4 s to ensure good adhesion to the build plate. Subsequent layers were printed with an exposure time of 2 s per layer.

Slot specimens were printed with the support material to allow uncured resin to drain from the slots and limit clogging. Therefore, the first four layers of slot specimens with increased exposure time were in the break-away support. For all other specimens, no support material was used. Slot specimen designs (Fig. 1) featured three rectangular pores with aspect ratios of 1:1, 3:1, and 5:1 arranged into three rows containing one of each and three columns. The longest dimension of each slot was parallel to the specimen length. Across the specimen width, the specified dimension of each slot was 0.22 mm with an average radius of curvature of 98  $\mu$ m. Slot heights were specified as 0.22, 0.66, and 1.11 mm. The slots were spaced 0.44 mm from each other and 0.22 mm from specimen edges. All specimens were washed with isopropyl alcohol and dried with compressed air.

Wedge specimens featured triangular-shaped wedges open on one end to promote directionally specific jetting. Three wedges





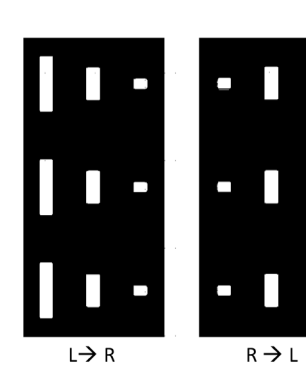


**FIG. 1.** Schematic of the AM polymer assemblies with the overall dimensions approximated and the impact direction designated (left-to-right and right-to-left) for the shock compression experiments.

were evenly spaced along the specimen length. The wedges extended 1.67 mm into the specimen width. At the open face, they measured 0.96 mm across and were spaced 0.74 mm apart. From the top and bottom edges, the wedges were spaced 0.84 mm. The tip of the wedge was 0.05 mm radius rather than a single point to accommodate the resolution of the printer.

# Shock compression experiments

Shock compression experiments were conducted at the Advanced Photon Source at the Dynamic Compression Sector.<sup>24</sup> Shockwaves were generated by launching an aluminum faced projectile with a gas gun coupled to time-resolved x-ray phase contrast imaging in order to monitor real-time deformation of the diode structure. In situ imaging of shockwave behavior in materials has been described in detail previously where 80-ps width x-ray bunches (24-bunch mode) with a peak photon energy of 25 keV spaced 153.4 ns apart were transmitted through the samples (exposure time of 60 ms) and detected using a LuAg:Ce (Lu<sub>3</sub>Al<sub>5</sub>O<sub>12</sub>:Ce) scintillator with ~55 ns decay time<sup>29</sup> optically coupled to four independent image intensified charge coupled device (ICCD) detectors (Princeton Instruments;  $\sim 20 \,\mu m$  pixel size, and  $1340 \times 1340$  pixels) and a 7× Mitutoyo infinity-corrected long working distance objective (Edmund NT46-144; 33.5 mm working distance and 3 µm focal depth) to provide up to eight x-ray images per experiment A schematic of the experwith a field of view of ~2.5 mm.2 imental setup is shown in Fig. 2.

The printed diode geometries were integrated into targets by affixing the polymer to an aluminum (Al 6061) base plate 1 mm in thickness and  $6 \times 6 \text{ mm}^2$  in side dimensions. The polymer architecture was backed by a polymethyl methacrylate (PMMA) window coated with an Al coating acting as a mirror in which photon Doppler velocimetry (PDV) was placed to measure the shockwave breakout time of the AM assembly. Additional PDV probes were incorporated into the target in order to measure the projectile velocity and the shockwave breakout of the Al baseplate, which coincides with the start of shock propagation into the AM assembly.

# EXPERIMENTAL RESULTS AND DISCUSSION

Finite element analysis was used to select configurations that produced the desired diode effect. A series of concepts was developed and analyzed to identify shapes that would produce jetting of material, and it was determined from model predictions that

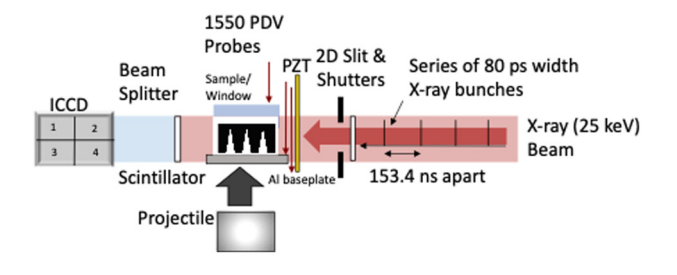


**FIG. 2.** Schematic of the x-ray phase contrast imaging coupled to a dynamic loading platform in order to generate shockwaves in polymer diode geometries.

configurations with shallow voids and gradual curvature are not likely to produce jetting behavior. Configurations with a deeper wedge shape at an angle 30° or less were predicted to form jets in the voided space. The final wedge configuration reported in this work was chosen based on the specimen size requirements for the PCI tests and feature size resolution limitations of the additive manufacturing method used to fabricate the specimens. Similar analysis was done on the slot configuration, which is an extension of work previously done on fractal geometries. The specific slot dimension assessed in this work was again selected based on the specimen size requirement but was mostly dictated by the limitations for printing internal void features.

# Wedge structures

To probe the directional behavior of the diode geometries, a nearly identical part was impacted in one direction  $(L \rightarrow R)$  and then the other  $(R \rightarrow L)$  and in situ phase contrast images recorded the shock propagation resulting from impact. Figure 3 shows the wedge configuration impacted left to right at  $u_0 = 0.697 \text{ km/s}$ , with the camera trigger times given for each frame with respect to impact (Fig. 3, top). The solid interface (no contrast) on the left side of the frame is the Al baseplate to which the printed sample is affixed. The PMMA window interface can be observed on the right side of the PCI image. In the first frame, there are artifacts designated by circles that are not due to the sample or the dynamic response but rather debris or defects on the Lexan windows incorporated in the gun target chamber. Also, the obstruction of the image on the top and bottom are a result of the heat chopper coming into the field of view during the experiment. The shockwave propagates into the sample, as seen in the first frame (left) and highlighted with an arrow. Rarefaction (release) waves are induced at the void-polymer interface, resulting in wave front interactions that slow the shockwave along the void-polymer interface compared with the bulk polymer. The lack of x-ray phase contrast at the shock front may be due to divergent waves dispersing the wavefront and lowering the density, or the shock front is tilted with respect to the direction of x-ray propagation, resulting in a significant reduction in contrast at the front. By contrast, a uniform shockwave with a distinct front is observed in the shocked bulk polymer (Fig. 6). In the third frame  $(4.390 \,\mu\text{s})$  with respect to impact), the triangular void begins to collapse, and wave fronts on either side of the void merge. In the final two frames, collapse of the void with material accumulation is observed. We note that the shockwave with a similar profile observed following the front is likely due to the imperfect glue bond seen in Fig. 3, top. The collapse of the gap along the glue bond between the Al baseplate and the AM polymer interface results in a second shock as the baseplate comes in contact with the polymer after the initial shock entered the wedge. Additionally, printing variations may be contributing to this second wavefront.

A similar printed sample was impacted in the opposite direction ( $R \rightarrow L$ ) at nearly the same impact velocity, and the shockwave localization behavior was observed by PCI in Fig. 3 (bottom). The wave front is uniform as it enters the polymer wedge as expected before propagating into the wedge features. Distortion of the shockwave can be seen at later times (4.366  $\mu$ s with respect to impact) where the uniform shockwave begins to slow due to release wave interactions at the void interface. As the shockwave propagates

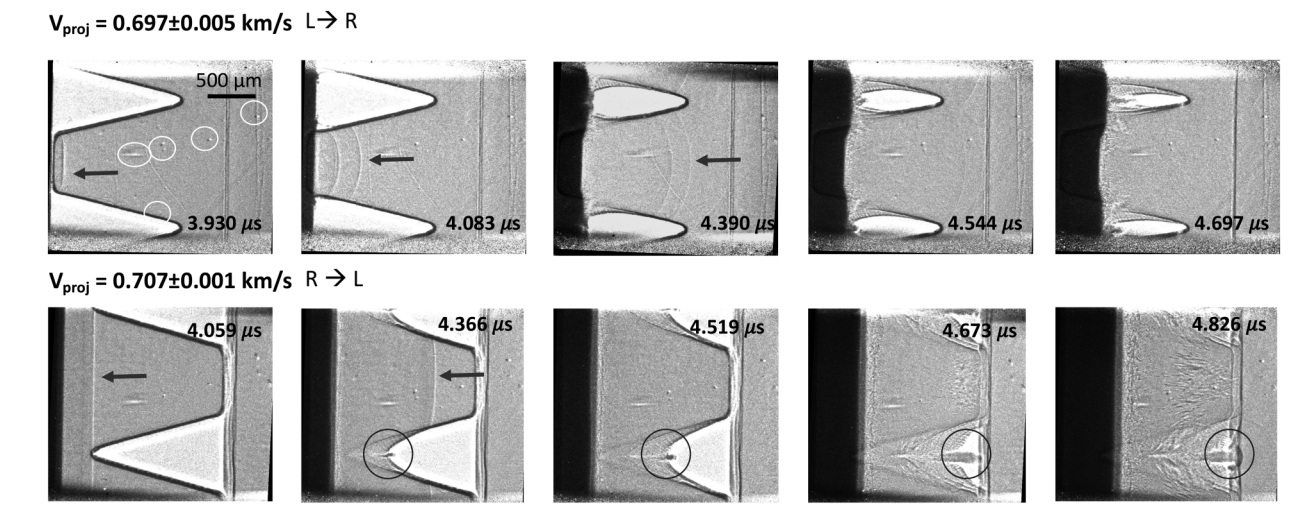


FIG. 3. Phase contrast images of the shockwave propagation in a wedge geometry with an impact direction from left to right (top) and right to left (bottom) at  $u_0 = 0.697$  km/s and 0.707 km/s, respectively. Camera times are given with respect to impact, with arrows designating shock front propagation and circles designating jet behavior.

through the void, a jet forms at the apex, indicated by a circle in Fig. 3 (bottom). The jet continues to grow in length until it impacts the PMMA window interface.

Similar diode assemblies were shocked at increased velocity  $(u_0\!\sim\!0.886\,km/s)$  as shown in Fig. 4. Similarly, a well-defined shock front propagates through the wedge depending on the impact direction, and jetting behavior is observed in the voids going from  $R\to L$  but absent in the reverse direction. We note the shock front in the  $R\to L$  case is more dispersed compared to the

opposite direction, and this is likely due to tilt with respect to the direction of the x-ray propagation.

At increased impact velocity, and shockwave pressure in the sample, it is noteworthy to point out the effects on the adjacent surfaces, i.e., the PMMA window where deformation is observed depending on the direction of impact. In the  $L \rightarrow R$  direction, the propagation of the final wave front into the PMMA window is consistent with shock attenuation, as observed by the lack of shock propagating into the witness PMMA window during deformation

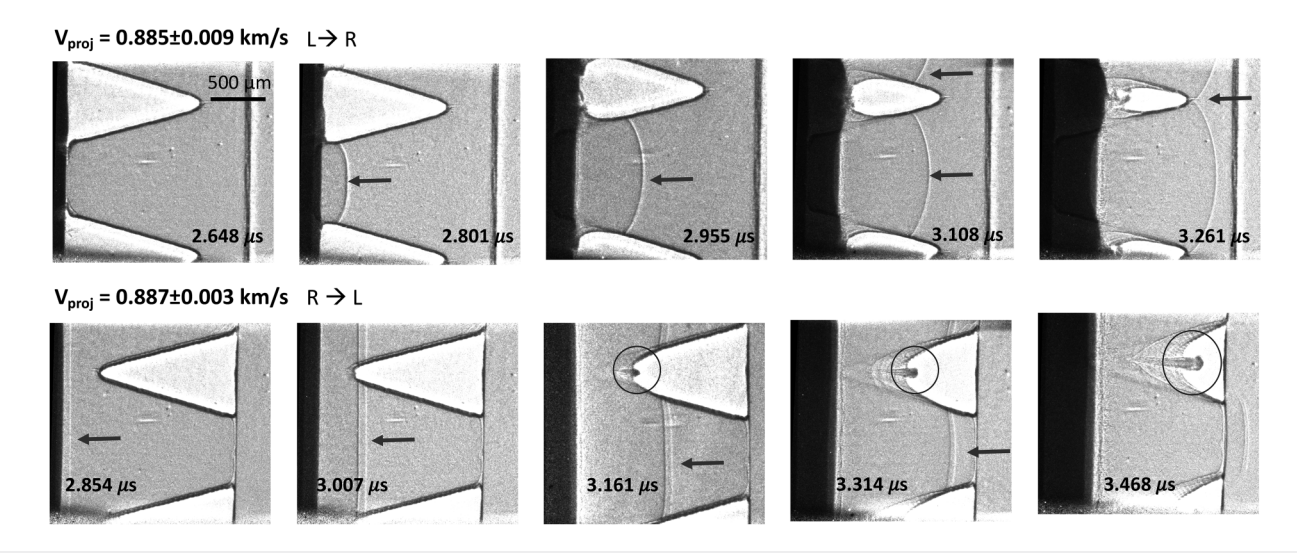


FIG. 4. Phase contrast images of the shockwave propagation in a wedge geometry with an impact direction from left to right (top) and right to left (bottom) at 0.885 km/s and 0.887 km/s, respectively. Camera times are given with respect to impact with arrows designating shock front propagation and circles designating jetting behavior.

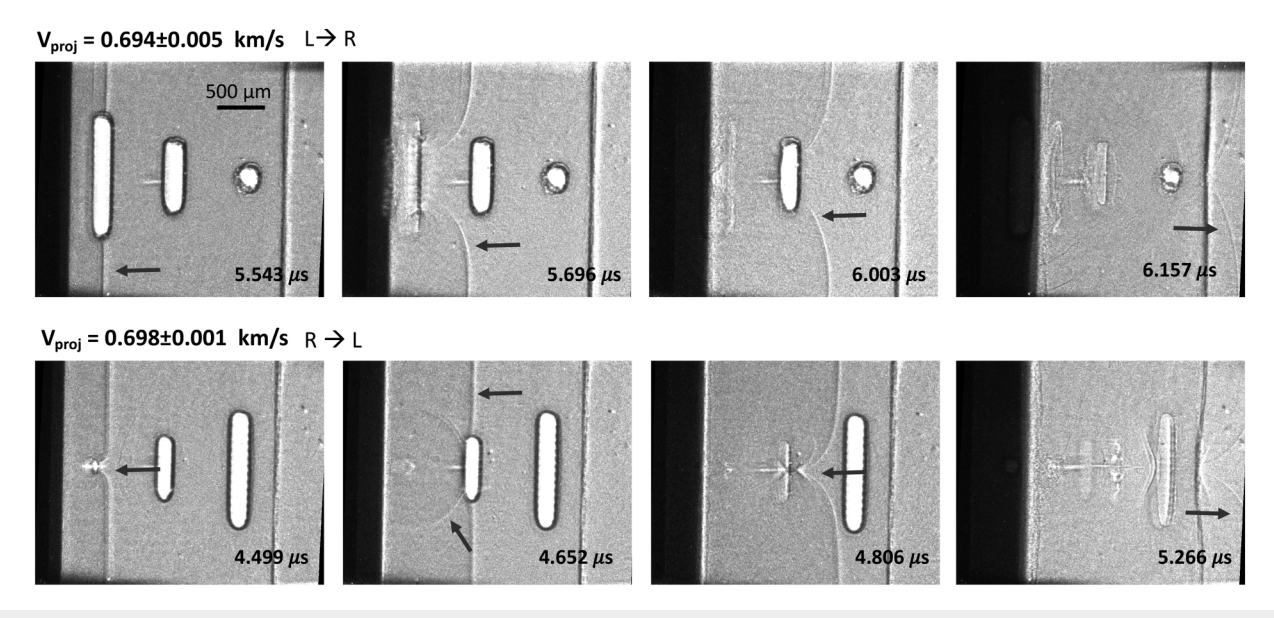


FIG. 5. Phase contrast images of the shockwave propagation in a slot geometry with an impact direction from left-to-right (top) and right-to-left (bottom) of 0.694 km/s and 0.698 km/s, respectively. Camera times are given with respect to impact with arrows designating shock front propagation in the polymer and PMMA window and rarefaction waves observed as a result of void collapse.

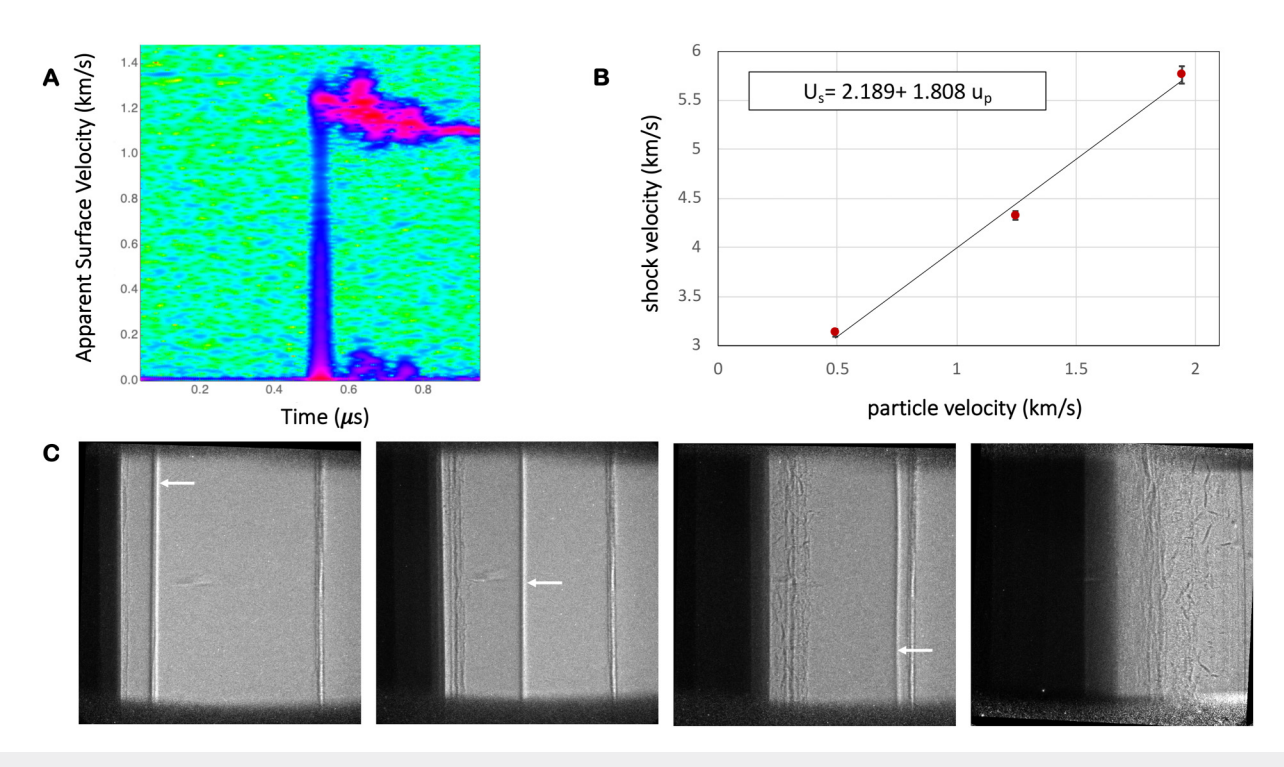


FIG. 6. (a) Measured photonic Doppler velocimetry (PDV) spectrogram of the transmitted wave in solid PR48 polymer resin impacted at (b) three impact velocities fitted to a linear Rankine–Hugoniot and the corresponding (c) phase contrast images of shock propagation.

**TABLE I.** Summary of measured projectile ( $u_0$ ), mass ( $u_p$ ), and shock ( $U_s$ ) velocities and calculated shock state pressures (P) from impact experiments on solid PR48 resin with initial density given ( $\rho_o$ ). PDV and PCI indicate whether the values came from the wave analysis of photonic Doppler velocimetry data or the dynamic x-ray phase contrast images, respectively. Errors in initial density, measured projectile, shock, and interface particle velocities (PDV) were propagated through the wave equations described by Mitchell and Nellis. <sup>32</sup>

Shot No.	Density $\rho_o$ (g/cm <sup>3</sup> )	Sample thickness (mm)	Projectile velocity, u <sub>0</sub> (km/s)	Particle velocity PCI, u <sub>p</sub> (km/s)	Particle velocity PDV, u <sub>p</sub> (km/s)	Shock velocity PCI, U <sub>s</sub> (km/s)	Shock velocity PDV, U <sub>s</sub> (km/s)	Pressure, P (GPa)
19-2-007 19-1-005	$1.18 \pm 0.010$ $1.18 \pm 0.010$	$2.021 \pm 0.0021$ $1.983 \pm 0.0010$	$0.68 \pm 0.0050$ $1.59 \pm 0.0034$	$0.51 \pm 0.038$ $1.31 \pm 0.069$	$0.49 \pm 0.029$ $1.25 \pm 0.027$	$3.01 \pm 0.03$ $4.11 \pm 0.036$	$3.13 \pm 0.039$ $4.33 \pm 0.044$	$1.8 \pm 0.3$ $6.3 \pm 0.2$
19-1-006	$1.18 \pm 0.010$	$2.019 \pm 0.0057$	$2.56 \pm 0.0047$	$2.23 \pm 0.039$	$1.94 \pm 0.030$		$5.76 \pm 0.088$	$13.2 \pm 0.2$

of the polymer assembly. In contrast, in the  $(R \to L)$  case, the jet impacts the PMMA surface and a strong shockwave enters the window material at  $3.65\,\mathrm{km/s}$  as predicted by FEM simulations shown below. This observation would not be possible with traditional velocimetry diagnostics; here, x-ray phase contrast imaging coupled to dynamic loading platforms enabled the observation of unique shockwave behavior in the materials of interest and the surrounding target hardware. These results further the knowledge base for the design of advanced shock mitigation materials incorporating directional behavior to eliminate damage to exterior components crucial to aviator, transportation, and military applications.

## Slot structures

In some applications, avoiding failure of the material may be required during shock loading. A novel slot diode geometry previously shown in Fig. 1 was developed in order to maintain directional behavior without failure or jetting. Figure 5 (top) shows the slot geometry impacted at  $u_0 = 0.694 \text{ km/s}$  from  $L \to R$  with the voids arranged from large-to-small dimensions. The initially uniform shockwave meets the first void that subsequently collapses causing the center of the shock front to diverge from planarity. The shock front on either side of the void continues through the bulk polymer and impacts the PMMA window before propagation at the center of the polymer can collapse the remaining void. The resulting shockwave profile in the PMMA material is a double wavelet curved at an angle of approximately 34° from the vertical PMMA interface as depicted schematically in Fig. 5. In comparison, if the slot diode is impacted from  $R \rightarrow L$  with the voids increasing in size, the distortion of the wave is significantly less until impacting the large slot, which prevents the shock from transmitting at the center of the void resulting in contraction of material in the last frame with the resulting shockwave in the PMMA steeper in angle with respect to the vertical (68°). Tailoring shockwave dynamics through the microstructure in polymer architectures has been previously reported; 19 but to our knowledge, achieving directional dependence through the design of novel architectures that incorporates diodelike behavior has not been previously reported. The slot diode assembly reported here modulates the shock behavior through the unique integration of voids. We observed this through PCI where localization occurs differently depending on the impact direction, and below FEM confirms modulation of the shock amplitude due to the divergence of the shockwave passing between sequentially narrower or wider slots (Fig. 13). This unique design is the first step toward more complex void geometries in order to achieve modulated or graded shock behavior in polymer materials.

In addition to the diode architectures investigated so far, shock compression experiments were conducted on the solid AM polymer material to measure the principal Hugoniot, providing data used to enable modeling of the commercially printed feedstock. Solid polymer assembles were affixed to an Al 6061 baseplate backed by a PMMA window. PDV and PCI measurements were made to obtain the particle velocity and the resulting shock velocity, as previously described. Figures 6(a) and 6(b) show the PDV spectrogram and the complimentary PCI images of the shockwave propagating (designated by arrow) through the solid polymer material for shot 19-2-005. The measured Hugoniot states from three impact experiments spanning shock pressures of 1.8–13.2 GPa are plotted in the shock velocity ( $U_s$ )-particle velocity ( $u_p$ ) plane in Fig. 6(c). A linear Rankine–Hugoniot fit to the data gives  $U_s = 2.189 + 1.808u_p$ . The data are summarized in Table I.

## MODELING RESULTS AND DISCUSSION

To gain additional insight into the measured behavior, numeric finite element analysis models of the tests were performed using Abaqus/Explicit, version 6.14. Models used a fully Eulerian approach with a fixed element size of  $10\,\mu\mathrm{m}$ . Plane strain conditions were assumed, reducing the model to a single layer of elements constrained to preclude motion in the out-of-plane direction. Material properties (Table II) were estimated from published data on similar materials,  $^{33-36}$  except for the  $U_s-u_p$  behavior of PR48, which used the  $U_s-u_p$  relationship defined in Fig. 6. All models used the as-designed geometry, 2.00 mm nominal thickness, and a uniform initial density of 1.173 g/cm<sup>3</sup>. We note that the as-measured density was calculated

TABLE II. Parameters used for constitutive models.

Property	Units	PR48	PMMA	Aluminum
Initial density	g/cm <sup>3</sup>	1.173	1.190	2.804
Elastic shear modulus	GPa	1.350	2.20	26.7
Yield strength	GPa	0.105	0.290	0.420
EOS—Reference sound	m/s	2189	2210	5200
speed, $c_0$				
EOS—slope, s		1.808	1.82	1.36
EOS—Grüneisen ratio, $\gamma_0$		1	0.85	2.2

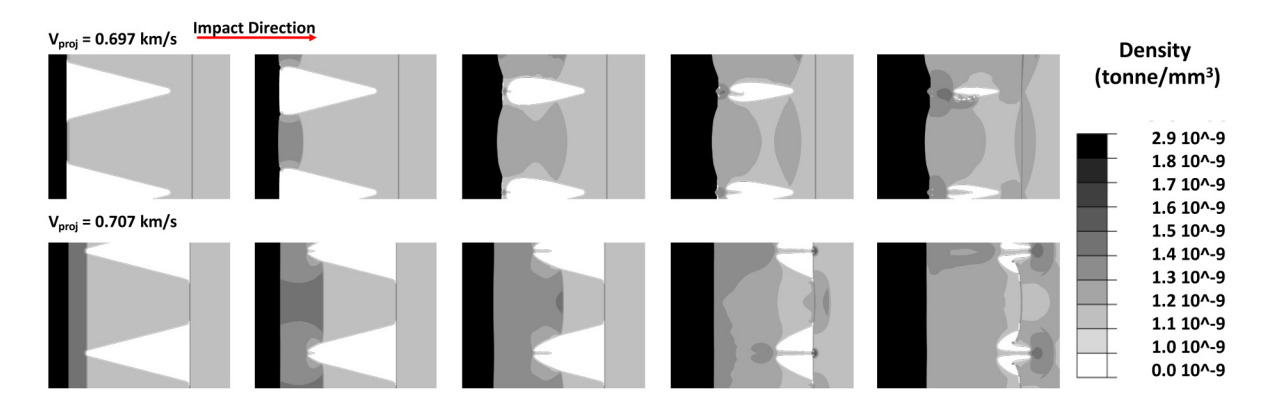


FIG. 7. Density contours predicted for the shock propagation in a wedge geometry with an impact direction from left-to-right (top) and right-to-left (bottom) at 0.697 km/s and 0.707 km/s, respectively.

from volume and mass and differs from the uniform initial density assumed in simulations but is within error. Also, the measured density was as much as 18% lower than the nominal density; this difference may explain some discrepancies between the measured and predicted response (Fig. 7).

Density contours predicted for the wedge-shaped configurations for impact velocities at 0.697 and 0.707 km/s are shown in Fig. 8. Timing of the left-most frame in each series was set to match that measured in the experiments, with time increments for subsequent images based on the progression of the FEA simulations.

The associated velocity contours are shown in Fig. 8. For wedge-shaped configurations at low (Fig. 8) and higher (Fig. 9) impact velocities, with a  $L \rightarrow R$  impact direction, several of the characteristics observed experimentally are captured in the

models; namely, the distortion of the shock front with the leading edge propagating faster at the center of the polymer in an arched profile and the collapse of the void. The models predict the accumulation of material within the void as it collapses in the form of a small jet, and although material accumulation is observed in the phase contrast images at later times, the feature is much less structured than the model predicts. To the contrary in the opposite (R  $\rightarrow$  L) direction of impact, shown in the lower portions of Figs. 8 and 9, a distinct jet of material is predicted to form in the void, which was readily observed in the experiment at both impact velocities (Figs. 3 and 4 shown previously). It is predicted that the jet results in a particle velocity that is similar to the shock velocity and is much higher than the expected particle velocity in the bulk material, which is typical for a highly distended material but more pronounced

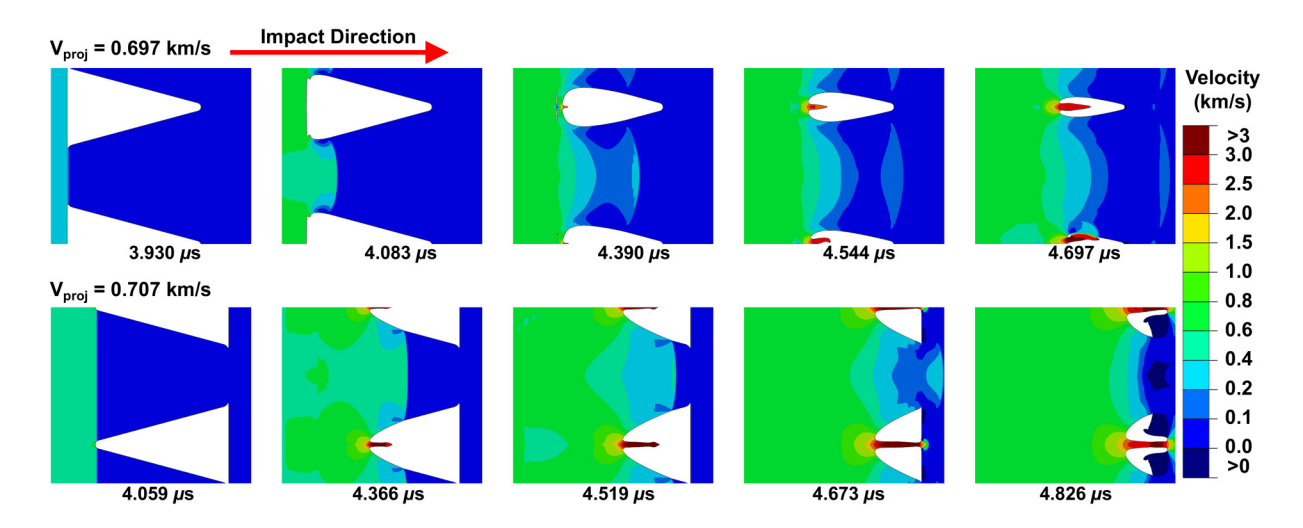


FIG. 8. Velocity contours predicted for the shock propagation in a wedge geometry with an impact direction from left-to-right (top) and right-to-left (bottom) at 0.697 km/s and 0.707 km/s, respectively.

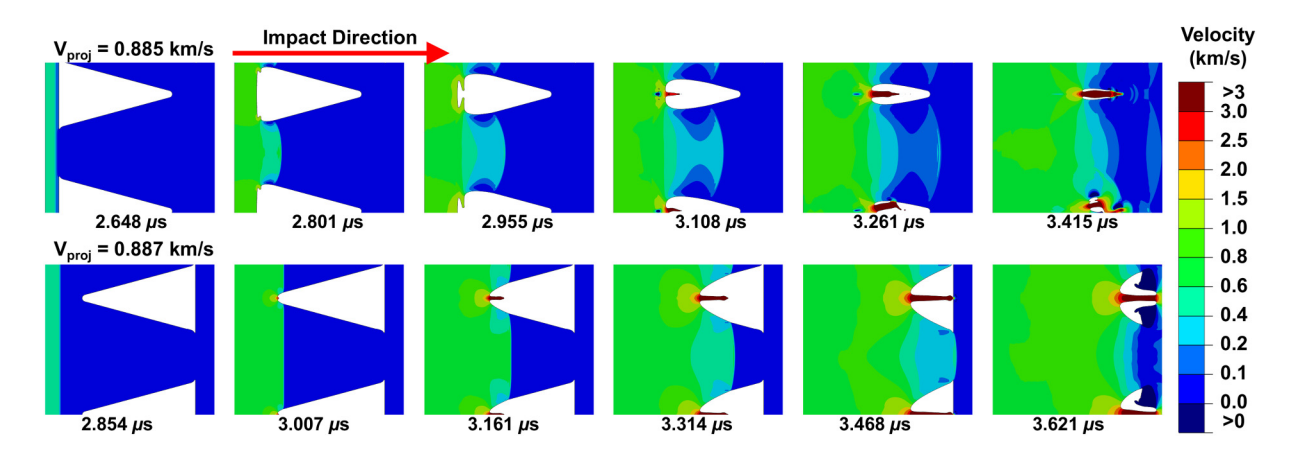


FIG. 9. Velocity contours predicted for the shock propagation in a wedge geometry with an impact direction from left-to-right (top) and right-to-left (bottom) at 0.885 km/s and 0.887 km/s, respectively.

here due to the wedge configuration of the polymer used for this testing and analysis. It is the coalescence of material in the wedge-shaped openings that pushes a jet forward, increasing the particle velocity to a much higher value than the velocity of the impacting projectile. Configurations that have other geometric features, such as semi-circular notches or triangular notches with higher interior angles than those reported in this paper, were analyzed (data not shown) and did not predict "jets" of material where the particle velocity increased significantly relative to the particle velocity in the bulk material. To illustrate this effect, at an impact velocity of 0.887 km/s, the bulk material has an expected shock velocity of 3.32 km/s and a particle

velocity of 0.692 km/s, while the particle velocity in the jet in Fig. 9 (bottom) is as high as 3.65 km/s. Additionally, while passing through the narrowing region between voids, the shock front is predicted to remain nearly planar for the right-to-left impact direction compared to a more distorted wave for the left-to-right shock front; both of these observations are qualitatively consistent with experiments.

The most-significant difference between the model predictions and the experiments for wedge-shaped configurations appears to be the prediction of jets that are more distinct, or the material in the jets is more clearly separated from the surrounding material compared to experimental. The most likely cause of this difference is

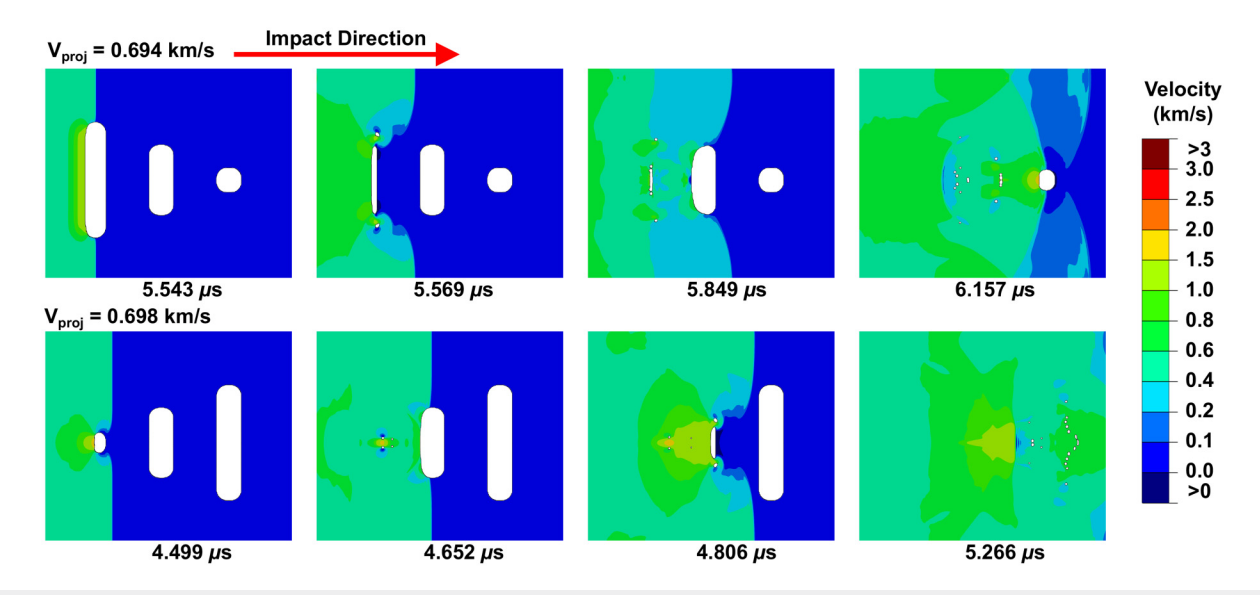


FIG. 10. Velocity contours predicted for the shock propagation in a slot geometry with an impact direction from left-to-right (top) and right-to-left (bottom) of 0.694 km/s and 0.698 km/s, respectively.

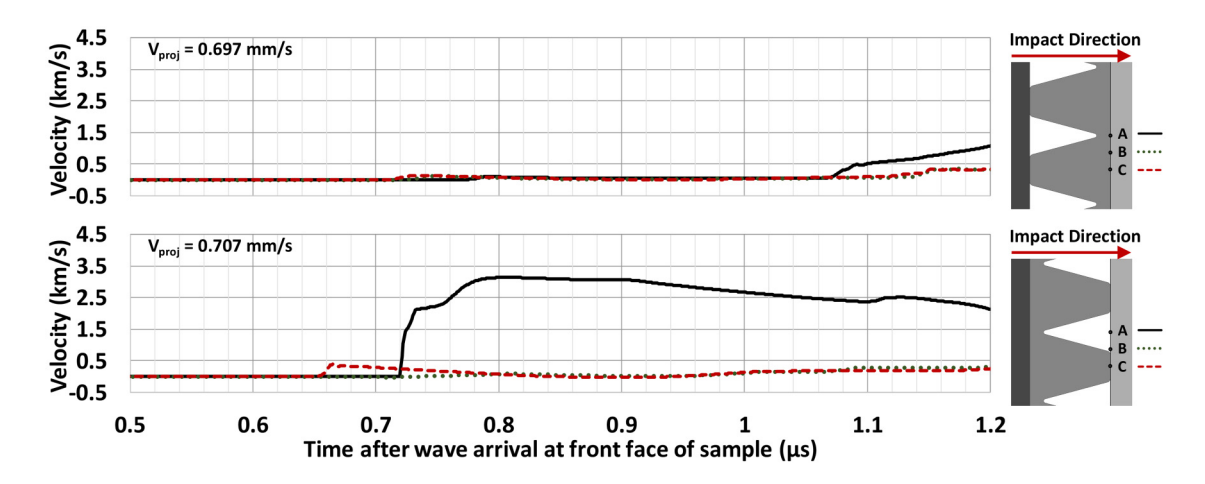


FIG. 11. Velocity histories predicted at three specific locations on the back face of a wedge geometry at the center of the void (a, black, continuous line), off-center of the void (b, green, dotted line), and in the bulk material (c, red, dashed line). Impact direction is from left-to-right (top) and right-to-left (bottom) at 0.697 km/s and 0.707 km/s, respectively.

the lack of complete densification of the material in the printed samples. Because the jet is more highly separated from the surrounding material in the models, the strength of the PR48 jet impacting the PMMA may be over-predicted by the models. This is evident due to the fact that the models predict jets that are narrower and penetrate more deeply into the PMMA than is observed in the phase contrast images. The narrowness and clear separation of the jets from the surrounding material that is predicted by the models imply that the impact of the jet as it strikes the back window is more highly localized in the models than in the measurements.

Similar to the wedge configuration, slot diode architectures impacted in both directions were simulated and are shown in Fig. 10. Predicted shock wave propagation through the slot configurations appears to match well with the phase contrast images. Similar to PCI, the shockwave evolution is dominated by void collapse release waves, which slow the shock front at the center of the diode structure.

To assess how the internal voids affect shock arrival at the PR48-PMMA interface, shock velocity histories were generated at specific locations in the FEA models. These were compared to the measured PDV traces (supplementary material). Figures 11–13

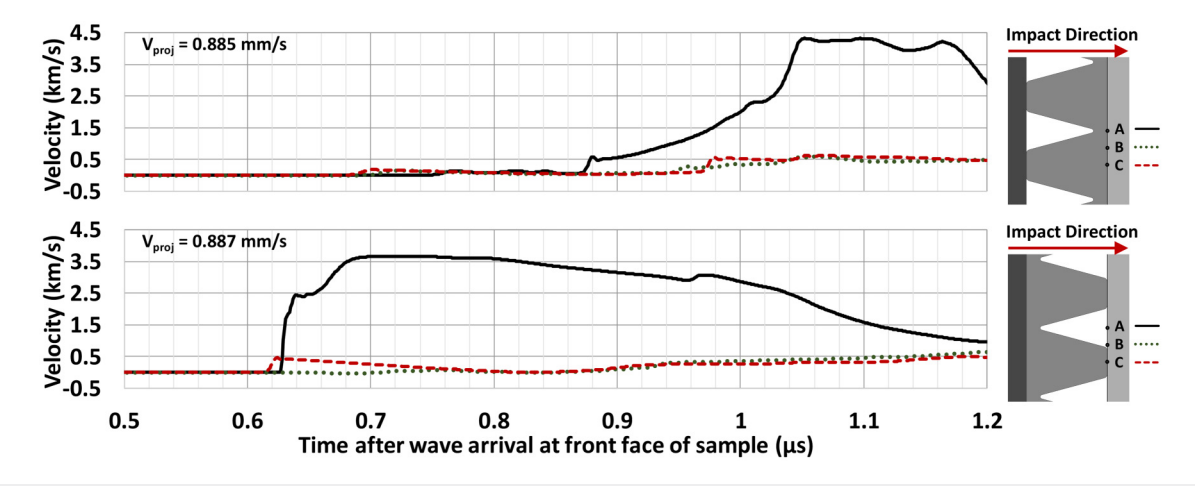
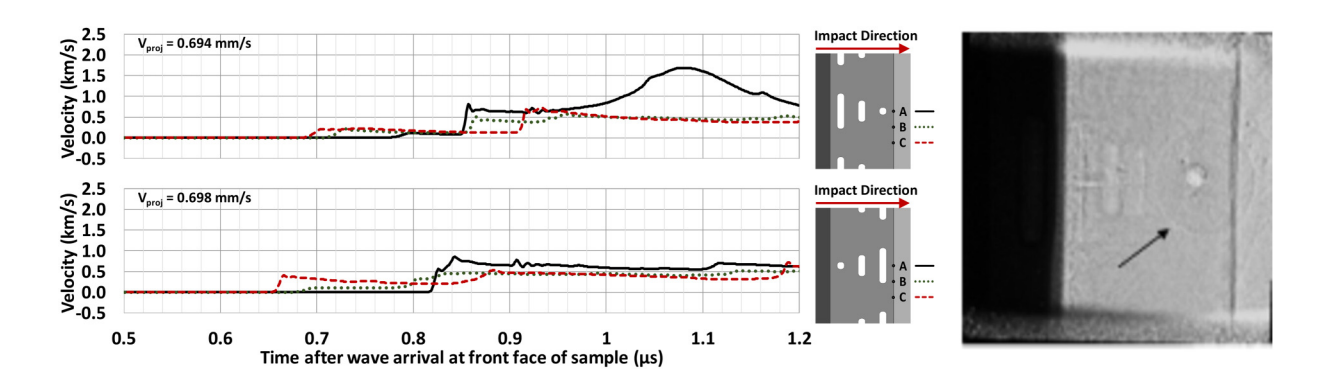


FIG. 12. Velocity histories predicted at three specific locations on the back face of a wedge geometry at the center of the void (a, black, continuous line), off-center of the void (b, green, dotted line), and in the bulk material (c, red, dashed line). Impact direction is from left-to-right (top) and right-to-left (bottom) at 0.885 km/s and 0.887 km/s, respectively.



**FIG. 13.** Velocity histories predicted at three specific locations on the back face of a slot geometry at the center of the voids (a, black, continuous line), off-center of the voids (b, green, dotted line), and in the bulk material (c, red, dashed line). Impact direction is from left-to-right (top) and right-to-left (bottom) at 0.694 km/s and 0.698 km/s, respectively. The corresponding PCI image is shown at the right with an arrow indicating the rarefaction wave resulting in a rise in velocity at  $0.85 \,\mu s$  with respect to impact also indicated by an arrow in the velocity history.

show velocity histories at three points in the models: point A is centered over the internal void feature, point C is centered between void features, and point B is halfway between A and C.

For comparison with the histories in Figs. 11 and 12, a solid monolithic sample of PR48 is predicted to have a rear surface interface velocity of 543 km/s for a projectile velocity of 700 km/s and 693 km/s for a projectile velocity of 900 km/s. For the wedge diode geometries, the velocities when the shock arrives at points B and C are significantly below that of a monolithic material, resulting from attenuation of the shock due to the internal features. Contrastingly, the velocity at point A rises to a level much higher than that in a monolithic sample but evolves differently depending on the direction of impact. For a  $L \rightarrow R$  (top) impact direction, collapse of the wedge-shaped void induces a ramp wave that gradually increases the velocity of the material at point A. Similar behavior was observed at higher impact velocity measured by PDV (supplementary material). For the  $R \rightarrow L$  impact direction, jetting of the material in the void region causes a rapid rise in shock velocity at point A, with pressures higher than those predicted for a shock traveling through a monolithic material. For example, pressures in a monolithic material impacted at 0.887 km/s are predicted to be 3.0 GPa when impacting the window, while pressures in a small region of the window impacted by the jet of the material in the R  $\rightarrow$  L wedge are predicted to exceed 6.0 GPa (for  $\approx$ 2 ns). As previously noted, the models may over-predict the jetting behavior, with lower velocities and pressures at point A in real samples than those indicated by these models. However, the jetting behavior or the absence thereof depending on the impact direction observed at point A experimentally through PCI and the resulting velocity simulated here is the first report of energy localization resulting from shockwave interactions of a void with directional dependence.

Velocity histories for the slotted configurations are shown in Fig. 13. At point C, the initial rise in velocity is associated with shock wave transmission through the PR48 polymer. Point B has a similar behavior but has a delayed arrival due to the interaction with the first void as observed previously in the PCI images where the shock front was slowed upon propagation into the void. The

amplitude of the initial rise in velocity at point C differs significantly depending on the impact direction due to the divergence of the shockwave passing between sequentially narrower and wider slots. At point A (Fig. 13, top), the initial rise in velocity, at  $0.78\,\mu s$ , results from direct transmission of the shock through the diode geometry. The larger rise in velocity at later time ( $0.85\,\mu s$ , Fig. 13 arrow) results from a rarefaction wave associated with the collapse of the adjacent short slot as indicated by the arrow in both the simulation and the PCI image to the right. At point A (Fig. 13, bottom), the longer slot adjacent to point A prevents the transmitted wave from propagating through the center of the polymer geometry, but a rise in shock velocity at  $0.82\,\mu s$  can be observed here and experimentally (Fig. 5) as a result of the shockwave associated with the collapse of the long slot.

The variations in the transmitted wave demonstrates the properties of the diode structures reported here with directional dependence of impact and localization effects that are observed laterally across the diode features (supplementary material). The geometries presented here offer tailored energy localization, which is important for explosive applications where microscale features can be used to tailor hotspot formation for initiation and detonation.<sup>37</sup>

# **CONCLUSIONS**

This work has demonstrated the use of engineered internal voids to control the localization and propagation of shockwaves through additively manufactured polymer structures. The unique placement and shape of the voids result in directionally dependent shock transmission including shock decay resulting from rarefaction waves at free surface interactions, ramped shockwave behavior due to pore collapse, and localization of material jetting. The shapes for the internal voids were selected based on the limited finite element analysis, but it is anticipated that with proper optimization and design, diode-like structures like those demonstrated in this work can be tailored further to more effectively augment shock transmission in one direction while diminishing transmission in

the other direction. The "shock diode" concept presented here is the first step toward developing functional shock materials for applications in which non-uniform shock loading may exist or augmented shock transmission is required.

#### SUPPLEMENTARY MATERIAL

See the supplementary material for photon Doppler velocimetry measurements of the diode geometries impacted  $L\to R$  and the opposing direction for the wedge geometry at  ${\sim}0.88\,\rm km/s$  and the slot geometry at 0.69 km/s. PDV shows the particle velocity attenuated in one direction with a slow ramp in velocity compared to the other direction for both configurations. Simulations were conducted to assess the effect of PDV probe placement on shock velocity.

#### **ACKNOWLEDGMENTS**

The authors would like to thank the staff at the Dynamic Compression Sector where compression experiments were performed, which is operated by Washington State University under the U.S. Department of Energy (DOE)/National Nuclear Security Administration under Award No. DE-NA0002442. Brittany Branch conducted this work under the support of C2 Science Campaign at Los Alamos National Laboratory and Sandia National Laboratories. Sandia National Laboratories is a multi-mission laboratory managed and operated by National Technology and Engineering Solutions of Sandia, LLC, a wholly owned subsidiary of Honeywell International Inc., for the U.S. Department of Energy's National Nuclear Security Administration under Contract No. DE-NA0003525. Additional Funding (Geoff Frank and Andrew Abbott) was made possible through Air Force Office of Scientific Research (AFOSR) under Project No. 16RXCOR326 (Martin Schmidt, Program Officer). Any subjective views or opinions that paper describes objective technical results and might be expressed in the paper do not necessarily represent the views of the U.S. Department of Energy or the United States Government.

# DATA AVAILABILITY

The data that support the findings of this study are available from the corresponding author upon reasonable request.

# **REFERENCES**

- <sup>1</sup>M. Jaffe, E. Baer, R. A. Dickie, C. D. Eisenbach, J. M. J. Frechet, J. P. Kennedy, J. L. Koenig, J. Kohn, D. A. Tirrell, I. M. Ward, C. G. Willson, and A. H. Windle, in *Applied Polymer Science 21st Century*, edited by C. D. Craver and C. E. Carraher (Pergamon, Oxford, 2000), p. 591.
- A. Dufresne, in Interface Engineering of Natural Fibre Composites for Maximum Performance, edited by N. E. Zafeiropoulos (Woodhead Publishing, 2011), p. 82.
   C. O. Oriakhi and M. M. Lerner, in Encyclopedia of Physical Science and Technology, 3rd ed., edited by R. A. Meyers (Academic Press, New York, 2003), p. 269.
- p. 269.

  <sup>4</sup>C. J. G. Plummer, in Reference Module in Materials Science and Materials Engineering (Elsevier, 2016).
- <sup>5</sup>N. Mills, Polymer Foams Handbook: Engineering and Biomechanics Applications and Design Guide (Butterworth-Heinemann, 2007).

- <sup>6</sup>C. C. Seepersad, J. K. Allen, D. L. McDowell, and F. Mistree, J. Mech. Des. 130, 031404 (2008).
- <sup>7</sup>D. W. Abueidda, R. K. Abu Al-Rub, A. S. Dalaq, D. W. Lee, K. A. Khan, and I. Jasiuk, Mech. Mater. **95**, 102 (2016).
- <sup>8</sup>E. Lind-Nordgren and P. Goransson, J. Sound Vib. 329, 753 (2010).
- <sup>9</sup>R. Yao, Z. J. Yao, J. T. Zhou, and P. J. Liu, J. Reinf. Plast. Compos. 35, 785 (2016).
- <sup>10</sup>A. Mirabolghasemi, A. H. Akbarzadeh, D. Rodrigue, and D. Therriault, Acta Mater. 174, 61 (2019).
- <sup>11</sup>A. M. Abou-Ali, O. Al-Ketan, R. Rowshan, and R. Abu Al-Rub, J. Mater. Eng. Perform. 28, 2316 (2019).
- <sup>12</sup>J. R. C. Dizon, A. H. Espera, Q. Y. Chen, and R. C. Advincula, Addit. Manuf. 20, 44 (2018).
- <sup>13</sup>I. Maskery, L. Sturm, A. O. Aremu, A. Panesar, C. B. Williams, C. J. Tuck, R. D. Wildman, I. A. Ashcroft, and R. J. M. Hague, Polymer 152, 62 (2018).
- <sup>14</sup>H. K. Peng, X. X. Wang, T. T. Li, S. Y. Huang, L. W. Wu, C. W. Lou, and J. H. Lin, J. Sandw. Struct. Mater. 21, 2512 (2019).
- <sup>15</sup>X. F. Cao, D. B. Xiao, Y. Li, W. B. Wen, T. Zhao, Z. H. Chen, Y. B. Jiang, and D. N. Fang, Thin-Walled Struct. 148, 106586 (2020).
- 16Z. C. Grasley and C. Leung, J. Eng. Mech. ASCE 137, 561 (2011).
- <sup>17</sup>J. Lind, B. J. Jensen, M. Barham, and M. Kumar, J. Mater. Res. 34, 2 (2019).
- <sup>18</sup>B. Branch, A. Ionita, B. M. Patterson, A. Schmalzer, B. Clements, A. Mueller, and D. M. Dattelbaum, Polymer **160**, 325 (2019).
- <sup>19</sup>B. Branch, A. Ionita, B. E. Clements, D. S. Montgomery, B. J. Jensen, B. Patterson, A. Schmalzer, A. Mueller, and D. M. Dattelbaum, J. Appl. Phys. 121, 135102 (2017).
- 20 J. E. Spowart, D. Lacina, C. Neel, G. Frank, A. Abbott, and B. Branch, "Shock propagation and deformation of additively-manufactured polymer foams with engineered porosity," in *Proceedings of the 2018 Annual Conference on Experimental and Applied Mechanics*, edited by Sharlotte Kramer, Jennifer L. Jordan, Helena Jin, Jay Carroll, and Alison M. Beese (Springer, 2020).
- <sup>21</sup>D. M. Dattelbaum, A. Ionita, B. M. Patterson, B. A. Branch, and L. Kuettner, AIP Adv. 10, 075016 (2020).
- <sup>22</sup>B. J. Jensen, S. N. Luo, D. E. Hooks, K. Fezzaa, K. J. Ramos, J. D. Yeager, K. Kwiatkowski, T. Shimada, and D. M. Dattelbaum, AIP Adv. 2, 012170 (2012).
- <sup>23</sup>S. N. Luo, B. J. Jensen, D. E. Hooks, K. Fezzaa, K. J. Ramos, J. D. Yeager, K. Kwiatkowski, and T. Shimada, Rev. Sci. Instrum. 83, 073903 (2012).
- <sup>24</sup>Y. Duan, X. H. Zhao, Z. Y. Liu, N. D. Hou, H. F. Liu, B. Du, B. Hou, and Y. L. Li, Compos. B Eng. 183, 107630 (2020).
- <sup>25</sup>L. J. Xiao, W. D. Song, and X. Xu, Thin-Walled Struct. 155, 106970 (2020).
- 26 Dassault Systemes, ABAQUS Documentation (2011).
- 27M. Molitch-Hou, see <a href="https://www.engineering.com/3DPrinting/3DPr
- <sup>28</sup>D. Capatina, K. D'Amico, J. Nudell, J. Collins, and O. Schmidt, AIP Conf. Proc. 1741, 030036 (2016).
- <sup>29</sup>M. Nikl, Meas. Sci. Technol. 17, R37 (2006).
- <sup>30</sup>J. Lind, B. J. Jensen, and M. Kumar, J. Mater. Res. 1979, 110008 (2018).
- 31 A. F. T. Leong, A. K. Robinson, K. Fezzaa, T. Sun, N. Sinclair, D. T. Casem, P. K. Lambert, C. J. Hustedt, N. P. Daphalapurkar, K. T. Ramesh, and T. C. Hufnagel, Exp. Mech. 58, 1423 (2018).
- <sup>32</sup>A. C. Mitchell and W. J. Nellis, J. Appl. Phys. **52**, 3363 (1981).
- 33K. Nakai and T. Yokoyama, J. Solid Mech. Mater. Eng. 6, 731 (2012).
- <sup>34</sup>A. Peterson, D. Bolling, G. Owolabi, E. Habtour, J. Riddick, and M. Coatney, Army Res. Lab. Tech. Rep., 2014.
- <sup>35</sup>D. Steinberg, Equation of State and Strength Properties of Selected Materials (Lawrence Livermore National Laboratory, 1996).
- 36G. Frank, University of Dayton Research Institute Technical Report UDR-TR-97-152, 1997.
- <sup>37</sup>F. P. Bowden and A. D. Yoffe, Am. J. Phys. **20**, 250 (1952).